



Contents lists available at ScienceDirect

## Remote Sensing of Environment

journal homepage: [www.elsevier.com/locate/rse](http://www.elsevier.com/locate/rse)

## Daytime fire detection using airborne hyperspectral data

Philip E. Dennison<sup>a,\*</sup>, Dar A. Roberts<sup>b</sup><sup>a</sup> Department of Geography and Center for Natural and Technological Hazards, University of Utah, Salt Lake City, UT 84112, USA<sup>b</sup> Department of Geography, University of California, Santa Barbara, CA 93106, USA

## ARTICLE INFO

## Article history:

Received 20 January 2009

Received in revised form 17 March 2009

Accepted 17 March 2009

## Keywords:

Wildfire detection

Hyperspectral

SWIR

AVIRIS

MODTRAN

## ABSTRACT

The shortwave infrared region of the electromagnetic spectrum, covering wavelengths from 1400 to 2500 nm, can include significant emitted radiance from fire. There have been relatively few evaluations of the utility of shortwave infrared remote sensing data, and in particular hyperspectral remote sensing data, for fire detection. We used an Airborne Visible InfraRed Imaging Spectrometer (AVIRIS) scene acquired over the 2003 Simi Fire to identify the hyperspectral index that was able to most accurately detect pixels containing fire. All AVIRIS band combinations were used to calculate normalized difference indices, and kappa was used to compare classification ability of these indices for three different fire temperature ranges. The most accurate index was named the Hyperspectral Fire Detection Index (HFDI). The HFDI uses shortwave infrared bands centered at 2061 and 2429 nm. These bands are sensitive to atmospheric attenuation, so the impacts of variable elevation, solar zenith angle, and atmospheric water vapor concentration on HFDI were assessed using radiative transfer modeling. While varying these conditions did affect HFDI values, relative differences between background HFDI and HFDI for 1% fire pixel coverage were maintained. HFDI is most appropriate for detection of flaming combustion, and may miss lower temperature smoldering combustion at low percent pixel coverage due to low emitted radiance in the shortwave infrared. HFDI, two previously proposed hyperspectral fire detection indices, and a broadband shortwave infrared-based fire detection index were applied to AVIRIS scenes acquired over the 2007 Zaca Fire and 2008 Indians Fire. A qualitative comparison of the indices demonstrated that HFDI provides improved detection of fire with less variability in background index values.

© 2009 Elsevier Inc. All rights reserved.

## 1. Introduction

Fire detection using remote sensing data has traditionally relied on two spectral regions: the thermal infrared (8–12  $\mu\text{m}$ ) and the middle infrared (3–5  $\mu\text{m}$ ) (e.g. Kaufman et al., 1990, 1998; Prins & Menzel, 1992; Giglio et al., 2003, Ichoku et al., 2003). As fire temperature increases, blackbody emission increases by temperature to the fourth power (Stefan–Boltzmann law) and shifts peak emission to shorter wavelengths (Wien's displacement law) (Fig. 1). At temperatures above 500 K, there is measurable emitted radiance in the shortwave infrared, the spectral region from 1400–2500 nm. At a temperature of 1150 K, the wavelength of peak emission is within the shortwave infrared. Despite ample fire emitted radiance in the shortwave infrared, this spectral region has been relatively underutilized for fire detection. Unlike the middle infrared and thermal infrared, fire detection in the shortwave infrared does not need to account for background emitted radiance (Fig. 1). However, daytime fire detection

in the shortwave infrared does have to contend with reflected solar radiance (Thomas & O, 1993).

Hyperspectral remote sensing data typically cover the visible (400–700 nm), near infrared (700–1400 nm) and shortwave infrared regions of the spectrum. In addition to capturing emitted radiance in the shortwave infrared, hyperspectral data possess narrow bands that may be appropriate for creating effective fire detection indices. An additional motivation for hyperspectral fire detection algorithms is to aid fire temperature retrieval. Hyperspectral data include detailed information on the spectral shape of emitted radiance, which can be modeled using radiative transfer by assuming blackbody emission. Green (1996) and Dennison et al. (2006) used linear spectral mixing techniques to model Airborne Visible InfraRed Imaging Spectrometer (AVIRIS) radiance spectra as a combination of background reflected solar radiance and emitted radiance at a specific temperature. This modeling approach is computationally intensive. Only a small percentage of image pixels typically contain fire, so a simple hyperspectral fire detection algorithm could allow temperature retrieval algorithms to run much more efficiently.

Two hyperspectral fire detection algorithms have been proposed (Vodacek et al., 2002; Dennison, 2006), but there have been no comprehensive, quantitative comparisons of potential hyperspectral

\* Corresponding author.

E-mail address: [dennison@geog.utah.edu](mailto:dennison@geog.utah.edu) (P.E. Dennison).

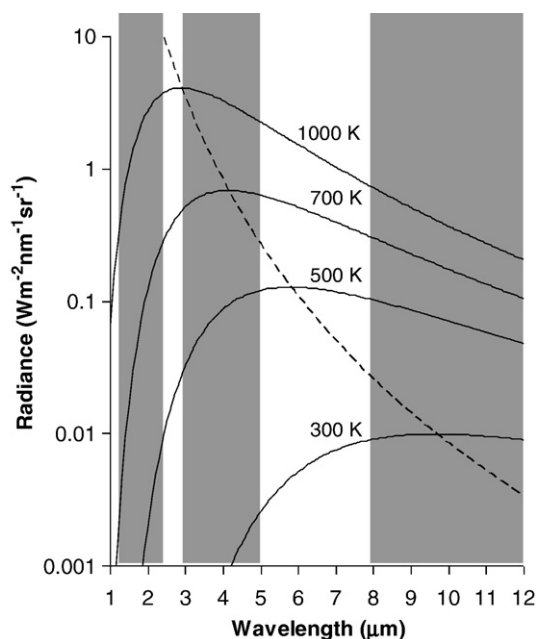


**Fig. 1.** Blackbody emission curves for temperatures of 300, 500, 700, and 1000 K. The black dashed line indicates the wavelength of peak emission, and the gray bars represent the approximate spectral extent (from left to right) of the shortwave infrared, middle infrared, and thermal infrared atmospheric windows. Note that not all wavelengths in these spectral regions have high transmittance.

fire detection indices. The objective of this research is to assess and compare potential daytime hyperspectral fire detection indices, with a focus on the shortwave infrared region of the spectrum. We used data from AVIRIS to evaluate thousands of normalized difference indices for fire detection, and used the MODTRAN radiative transfer model to analyze the sensitivity of the best index to varying conditions.

## 2. Background

### 2.1. Fire detection using the shortwave infrared

Operational fire detection algorithms use middle infrared and thermal infrared bands for fire detection, but can also utilize shorter wavelength bands, including the shortwave infrared, for contextual screening for false detections (e.g., Giglio et al., 2003). Fire detection algorithms that specifically take advantage of shortwave infrared emitted radiance have been developed for Advanced Spaceborne Thermal Emission and Reflection Radiometer (ASTER) and Moderate Resolution Imaging Spectroradiometer (MODIS) data. ASTER has six shortwave infrared bands with 30 m spatial resolution, while MODIS has two 500 m spatial resolution bands covering wavelengths longer than 1400 nm. Morisette et al. (2005a) used shortwave infrared ASTER data for validation of a standard MODIS fire detection product in southern Africa. They found a fixed threshold for ASTER band 9 (2.4 μm) radiance data that allowed reliable discrimination of fire emitted radiance and cloud-reflected solar radiance. Morisette et al. (2005b) developed a refined ASTER fire detection algorithm that converts bands 8 (2.33 μm) and 3 (0.82 μm) to reflectance, and then examines the ratio of and difference between band reflectance values to detect fire. ASTER fire detections derived using this algorithm have been applied to validating standard MODIS fire detection products in the Brazilian Amazon (Morisette et al., 2005b; Schroeder et al., 2008) and Siberia (Csiszar et al., 2006). Giglio et al. (2008) evaluated this same approach for daytime time detection, and band 8 alone for nighttime fire detection, on 100 ASTER scenes from nine different global regions.

Wang et al. (2008) examined use of a Normalized Multi-band Drought Index (NMDI) for detecting fires in MODIS data. The NMDI uses MODIS band 2 (0.86 μm), 6 (1.64 μm), and 7 (2.13 μm) reflectance, and was originally intended as a measure of vegetation moisture status (Wang & Qu, 2007). They found that increased shortwave infrared emission from fires led to abnormally depressed NMDI values, allowing for detection of forest fires in MODIS data covering an area of the southeastern USA. While these studies found that shortwave infrared data were useful for fire detection, they were restricted to using wavelengths measured by ASTER and MODIS bands. Hyperspectral data have narrow bands and cover a much wider range of wavelengths. Also, hyperspectral data could be used to determine whether there are more optimal shortwave infrared bands that can be used for fire detection.

### 2.2. Hyperspectral fire detection indices

Two hyperspectral fire detection indices have been previously proposed. Vodacek et al. (2002) noted sharp potassium emission lines at 767 nm and 770 nm as a signature of burning biomass. They developed a potassium emission index using the ratio of a band containing the emission lines and a reference band:

$$\text{potassium emission index} = \frac{L_{770}}{L_{780}} \quad (1)$$

where  $L$  indicates radiance from a band centered on the subscript wavelength, in nm. Index values increase with the presence of fire within a pixel. Vodacek et al. (2002) used the potassium emission index to detect fires in AVIRIS data acquired over the Brazilian Amazon. Dennison (2006) proposed a shortwave infrared algorithm based on carbon dioxide absorption at 2010 nm. The depth of this carbon dioxide absorption feature decreases as emitted radiance from a fire is added to the total radiance measured by a sensor. The Dennison (2006) carbon dioxide absorption index uses two reference bands:

$$\text{carbon dioxide absorption index} = \frac{L_{2010}}{0.666 \cdot L_{1990} + 0.334 \cdot L_{2040}} \quad (2)$$

Dennison (2006) used this index to demonstrate fire detection in AVIRIS and Hyperion data. Both the Vodacek et al. (2002) and Dennison (2006) indices rely on relatively narrow spectral features, and are sensitive to hyperspectral band width and placement. While both of these studies introduced viable hyperspectral fire detection indices, they evaluated only a small fraction of the potentially useful bands that hyperspectral data can provide.

## 3. Methods

### 3.1. Evaluating hyperspectral fire detection indices

To derive candidate fire detection indices, we used a map of fire temperature generated from AVIRIS radiance data covering the 2003 Simi Fire in southern California (Dennison et al., 2006). AVIRIS collects 224 contiguous bands with 10 nm bandwidths covering an approximate spectral range of 370–2510 nm. Precise radiometric calibration of the AVIRIS instrument permits accurate quantification of at-sensor radiance (Green et al., 1998). Dennison et al. (2006) used blackbody emitted radiance endmembers ranging in temperature from 500 to 1500 K, along with background reflected solar radiance endmembers, to model the dominant temperature of emission for each pixel in the scene. MODTRAN (Berk et al., 1989) was used to correct the emitted radiance endmembers for atmospheric attenuation, and the best fit combination of emitted radiance and reflected solar radiance was fit to each pixel using multiple endmember spectral mixture analysis (Roberts et al., 1998). This technique produced maps of fire temperature (Fig. 2), per pixel fire fractional area, and background

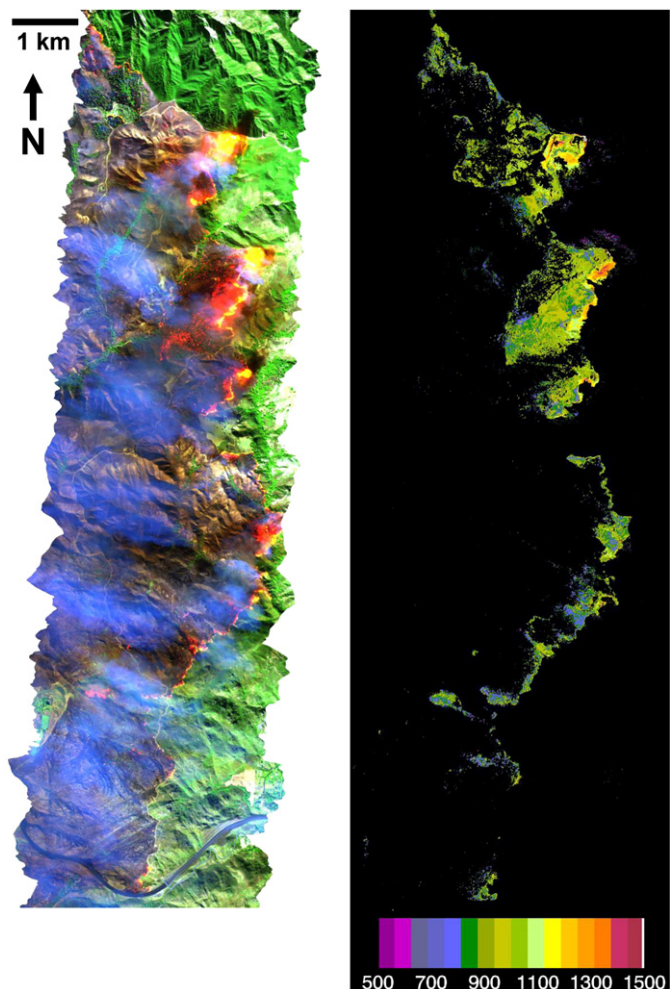


Fig. 2. A SWIR-NIR-red false color composite of an AVIRIS scene collected over the Simi Fire on October 27, 2003 (left); and fire temperature, in Kelvin, modeled from the same scene by Dennison et al. (2006) (right).

land cover. Approximately 9% of the AVIRIS scene was found to have a significant contribution from an emitted radiance endmember (Dennison et al., 2006). The fire temperature map revealed a relatively small number of pixels along the fire front that contained high temperature emission. A much larger area behind the fire front contained lower temperature emission, likely due to small fires and smoldering combustion (Fig. 2). Fire fractional area was less than 10% for most areas of the fire, but exceeded 50% in a few pixels along the fire front (Dennison et al., 2006).

Since blackbody emission changes with temperature, the utility of fire detection indices may also change with temperature. We used the Dennison et al. (2006) temperature map to create four image masks for the AVIRIS Simi Fire radiance data. A non-burning mask selected pixels with no modeled emitted radiance. The first temperature mask selected all pixels modeled with a fire temperature, covering a range from 500 to 1500 K. The second and third temperature masks selected lower temperature pixels, since reduced emission from these pixels may make fire detection more difficult. The second temperature mask selected pixels with temperatures from 500 to 1000 K, and the third temperature mask selected pixels with the coolest fires, ranging from 500 to 750 K. The number of pixels in each mask is shown in Table 1. AVIRIS pixels containing saturated bands were excluded from the temperature masks, since the true spectral shape of their emitted radiance could not be determined.

We used the normalized difference index (NDI) equation to calculate candidate fire detection indices from the masked AVIRIS radiance

data covering the Simi Fire. Our normalized difference indices have the form:

$$NDI(\lambda_1, \lambda_2) = \frac{(L_{\lambda_1} - L_{\lambda_2})}{(L_{\lambda_1} + L_{\lambda_2})} \quad (3)$$

where  $L_{\lambda_1}$  is the radiance of the band centered on wavelength  $\lambda_1$ , and  $L_{\lambda_2}$  is the radiance of the band centered on wavelength  $\lambda_2$ . The NDI equation was selected since it can be rapidly calculated, and because the bounding values of  $-1$  and  $1$  facilitate easy interpretation. Normalized difference indices were calculated for all possible combinations of AVIRIS bands, for all pixels within the Simi Fire scene. With 224 AVIRIS bands, there are 24,976 unique band combinations not counting transposition of  $\lambda_1$  and  $\lambda_2$  and indices where  $\lambda_1$  equals  $\lambda_2$ .

All of the candidate normalized difference indices were used to classify the AVIRIS radiance image for the following three cases:

- non-burning vs. burning at any temperature
- non-burning vs. burning at temperatures below 1000 K
- non-burning vs. burning at temperatures below 750 K

A threshold separating non-burning from burning was empirically determined for each NDI and for each of the above cases using the kappa statistic (Cohen, 1960). Kappa was calculated from a classification error matrix of non-burning vs. burning pixels, and used to determine fire detection accuracy. Unlike overall accuracy, kappa accounts for agreement by chance and is a better measure of accuracy when one class (in this case, non-burning pixels) dominates a classified image (Congalton, 1991). Kappa ranges between 0 and 1, with 0 indicating no agreement and 1 indicating total agreement. The detection threshold for each NDI and range of temperatures was determined by finding the threshold that produced the highest kappa value. The resulting kappa value represents the maximum accuracy for each combination of bands and range of temperatures. Since saturation typically occurred only in shortwave infrared bands, exclusion of pixels containing saturated bands will increase the kappa values of indices using these bands, while potentially decreasing the kappa values of indices that use shorter wavelength non-saturated bands that may function better at higher emitted radiance. The NDI that had the highest accuracy for all three temperature ranges was selected for application to the Simi Fire AVIRIS scene and for modeling index sensitivity.

### 3.2. Index sensitivity modeling

The selected index (henceforth referred to as the hyperspectral fire detection index, or HFDI) uses bands containing atmospheric trace gas absorption, and is thus sensitive to variations in path length and trace gas concentrations. MODTRAN was used to model index sensitivity to three varying conditions: elevation, solar zenith angle, and atmospheric water vapor concentration. First, conditions during the Simi Fire were simulated using the parameters listed in Table 2. MODTRAN was used to create synthetic radiance spectra based on the reflectance curve of the ash background endmember selected by Dennison et al. (2006), plus modeled blackbody emitted radiance. Both temperature

Table 1  
Number of pixels in each image mask applied to the AVIRIS Simi Fire radiance image.

Class	Number of pixels
Non-burning	1,781,073
All temperatures	143,853
T < 1000 K	105,426
T < 750 K	8504

**Table 2**  
AVIRIS scene properties for each fire.

Fire name	Simi	Zaca	Indians
Scene date	27 Oct 2003	12 Aug 2007	11 Jun 2008
Latitude	34.33°	34.62°	36.07°
Longitude	−118.65°	−119.78°	−121.38°
Mean scene time (UTC)	21:06	21:52	20:52
Mean solar zenith angle	52.5°	31.3°	26.4°
Mean ground elev. (m)	650	710	776
Sensor elev. (km)	5.6	5.6	19
Approx. spatial resolution (m)	4	3.8	16
Mean atmospheric water vapor concentration (atm cm)	926	1435	443

Mean atmospheric water vapor concentration was determined using ACORN (ImSpec LLC).

and fire fractional area were varied to create a synthetic image of 101 by 101 pixels. Temperature was varied from 500 to 1500 K in 10 K increments. Fire fractional area was varied from 0 to 100% in 1% increments. A nadir view zenith angle was assumed in all cases. HFDI was calculated for each of the 10,201 spectra in the resulting synthetic image, allowing evaluation of index response over a wide range of temperatures and fire fractional areas.

To determine index sensitivity to elevation, solar zenith angle, and water vapor concentration, one of these parameters was varied while the remaining parameters were fixed to the values for the Simi Fire AVIRIS scene (Table 2). The sensitivity of the HFDI to elevation was tested at elevations of 0, 1, 2, and 3 km. The sensitivity of the HFDI to solar

**Table 3**  
The five band combinations and thresholds with the highest Kappa values for pixels emitting at any temperature.

Bands	Wavelengths (nm)	Threshold	Kappa	Overall accuracy
216, 178	2429, 2051	−0.01	0.7943	97.27%
216, 180	2429, 2071	−0.02	0.7938	97.27%
216, 179	2429, 2061	−0.04	0.7936	97.26%
221, 173	2479, 2000	−0.01	0.7914	97.19%
219, 179	2459, 2061	0.01	0.7905	97.21%

The longer wavelength band is used as  $\lambda_1$  from Eq. (3) in all cases, so that pixels containing fire have higher index values than pixels that do not contain fire.

**Table 4**  
The five band combinations and thresholds with the highest Kappa values for pixels emitting at temperatures less than 1000 K.

Bands	Wavelengths (nm)	Threshold	Kappa	Overall Accuracy
216, 179	2429, 2061	−0.06	0.7875	97.93%
219, 175	2459, 2021	−0.21	0.7872	97.90%
219, 173	2459, 2000	−0.27	0.7871	97.90%
213, 179	2399, 2061	−0.08	0.7861	97.91%
220, 173	2469, 2000	−0.17	0.7860	97.90%

The longer wavelength band is used as  $\lambda_1$  from Eq. (3) in all cases, so that pixels containing fire have higher index values than pixels that do not contain fire.

zenith angle was evaluated at solar zenith angles of 0°, 25°, 50°, and 75°. Finally, the sensitivity of the HFDI to water vapor was examined for water vapor concentrations of 500, 1000, 1500, and 2000 atm cm.

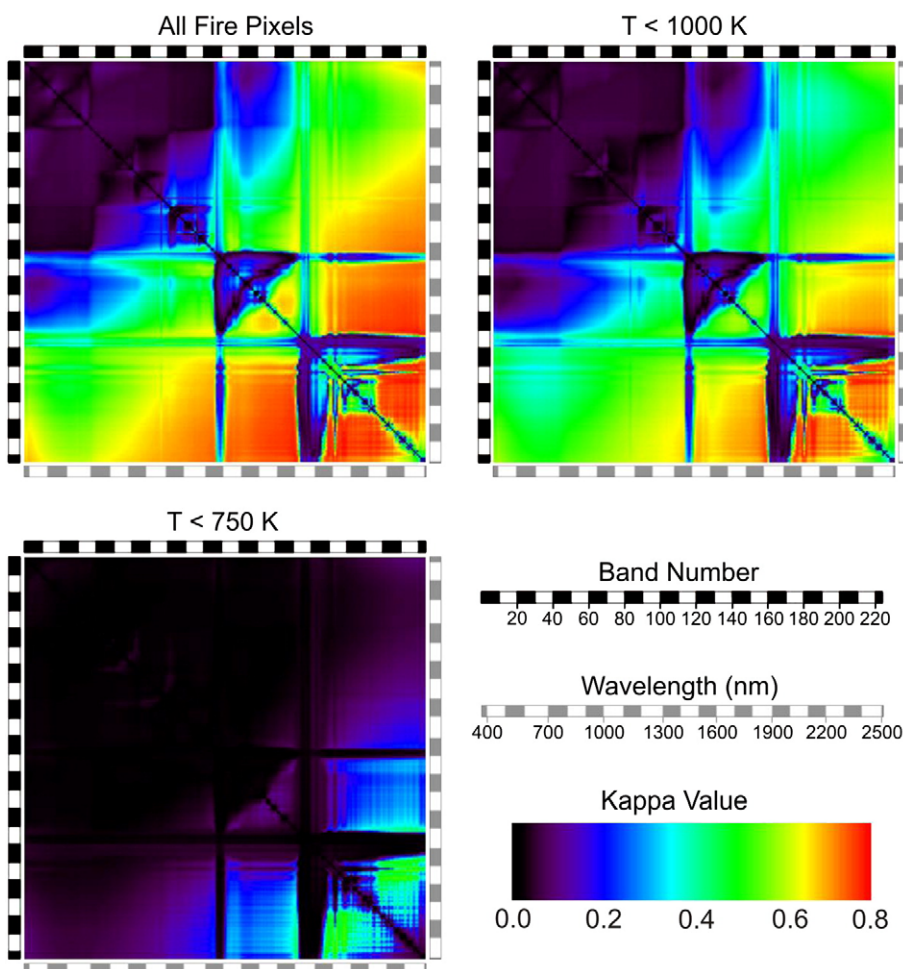


**Fig. 3.** Kappa matrices for normalized difference indices using bands  $i$  and  $j$ , where band  $i$  is the row number and band  $j$  is the column number. Kappa matrices are shown for classifications of all fire pixels (top left), fire pixels with a temperature less than 1000 K (top right), and fire pixels with a temperature less than 750 K (bottom left). The black shaded bars to the top and left of each matrix show band number, and the gray shaded bars to the bottom and right of each matrix show approximate wavelength.

**Table 5**

The five band combinations and thresholds with the highest Kappa values for pixels emitting at temperatures less than 750 K.

Bands	Wavelengths (nm)	Threshold	Kappa	Overall Accuracy
216, 175	2429, 2021	−0.35	0.5421	99.67%
219, 175	2459, 2021	−0.29	0.5416	99.67%
217, 175	2439, 2021	−0.29	0.5388	99.67%
220, 175	2469, 2021	−0.20	0.5383	99.67%
215, 175	2419, 2021	−0.25	0.5377	99.67%

The longer wavelength band is used as  $\lambda_1$  from Eq. (3) in all cases, so that pixels containing fire have higher index values than pixels that do not contain fire.

### 3.3. Comparison of hyperspectral fire detection indices

The HFDI was applied to AVIRIS scenes acquired over the 2007 Zaca Fire in southern California and over the 2008 Indians Fire in central California. Metadata for these AVIRIS scenes are listed in Table 2. Two additional hyperspectral indices were calculated from these AVIRIS scenes: the Vodacek et al. (2002) potassium emission index, and the Dennison (2006) carbon dioxide absorption index. The AVIRIS radiance data were also corrected to apparent surface reflectance using ACORN (ImSpec LLC) and convolved to match the ASTER sensor response function using ENVI (ITT Industries Inc.). The Morissette et al. (2005b) fire detection index using the ratio of ASTER band 8 (2300–2370 nm) to band 3 (760–860 nm) was then calculated from the simulated ASTER reflectance data. Images of all four indices were qualitatively compared to determine the best index for fire detection in these AVIRIS scenes.

## 4. Results

The matrices in Fig. 3 display kappa values for the 24,976 unique combinations of AVIRIS bands. The diagonal line from the upper-left to lower-right corner of each matrix marks where each NDI is equal to zero because the same band is used in the NDI twice. The kappa values to the lower-left of this line are a reflection of the kappa values to the upper-right, due to reselection of the same bands but in reverse order.

All three matrices feature low kappa values for indices that utilize visible and near infrared bands (Fig. 3). Emitted radiance is relatively low in these spectral regions, while reflected solar radiance relatively

high. Also, smoke is an efficient scatterer and absorber of emitted radiance in the visible and near infrared, greatly reducing classification accuracy for indices using bands in these spectral regions. There is no indication of increased kappa values for indices using the 770 nm potassium emission feature (Vodacek et al., 2002) for any of the temperature ranges. Kappa values increased for bands in the short-wave infrared, with the highest accuracies for all three temperatures residing between 1900 and 2500 nm. Kappa values were generally higher for the full temperature range, and decreased as the temperature range decreased. For both the full temperature range and for temperatures less than 1000 K, kappa values peaked just below 0.8 (indicated by the red colors). In contrast, the kappa values for temperatures less than 750 K were much lower, peaking above a more modest 0.5 (indicated by green colors). As fire temperature decreases, emitted radiance also decreases, making pixels containing lower temperature emission more difficult to detect.

In all three kappa matrices there is visible “structure” caused by atmospheric trace gas absorption features in the shortwave infrared. Strong atmospheric water vapor absorption features near 1400 and 1900 nm produced very low kappa values. The carbon dioxide absorption doublet centered on 2010 and 2060 nm increased kappa values, except at the maximum of the 2010 nm absorption where total radiance was relatively low. NDI using the 2010 nm band (previously

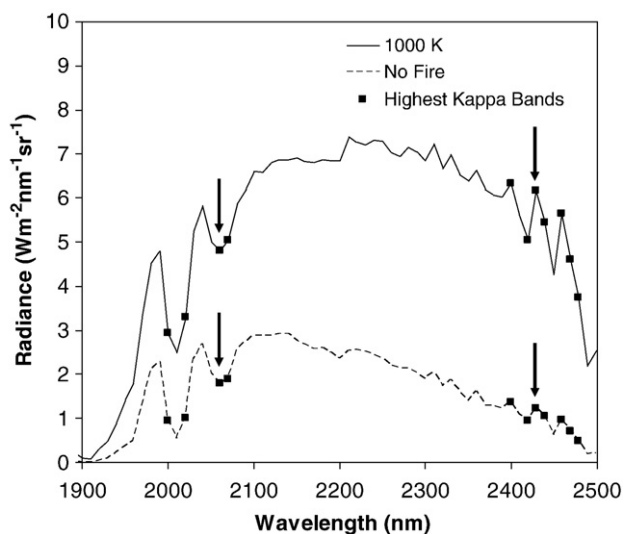


**Fig. 4.** This plot shows AVIRIS-measured radiance for a pixel modeled with a 1000 K fire and a pixel modeled with no fire. The bands listed in Tables 2–4 are marked as boxes on the radiance curve. Arrows indicate the 2061 and 2429 nm bands selected for the HFDI.

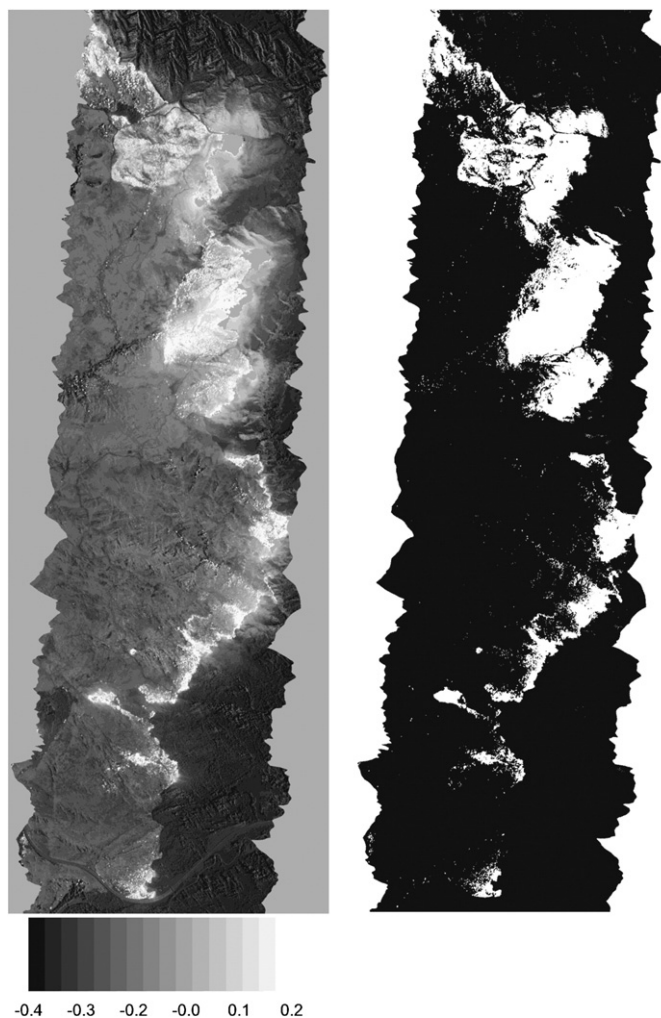


**Fig. 5.** Values of the HFDI calculated using bands 216 (2429 nm) and 179 (2061 nm) for the Simi Fire AVIRIS scene are shown in the left image. Pixels selected as containing fire based on an index threshold of  $-0.04$  are shown as white in the right image.

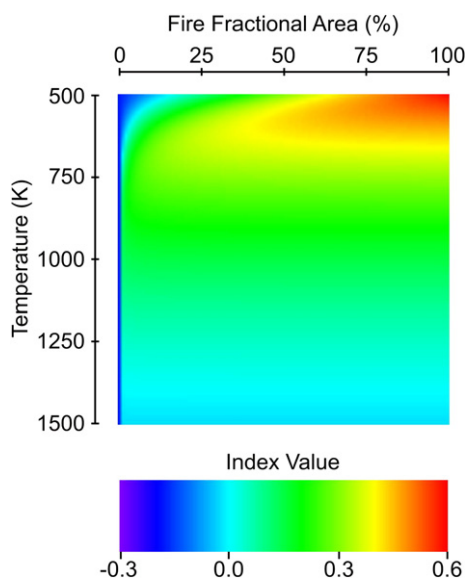


**Fig. 6.** HFDI values modeled for the Simi Fire AVIRIS scene using MODTRAN. Fire fractional area increases at 1% increments moving from left to right, and temperature increases with 10 K increments moving from top to bottom.

used by Dennison (2006)) had markedly lower kappa values, likely due to lower signal. Alternating bands of higher and lower kappa values beyond 2300 nm were caused by water vapor and methane absorption features. Kappa values were highest at absorption minima and lowest at absorption maxima.

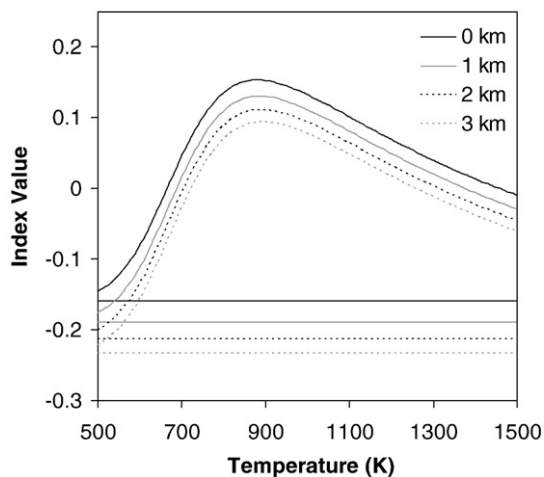


**Fig. 8.** HFDI values across a range of temperatures for elevations of 0, 1, 2, and 3 km. The lower, flat lines indicate index values at 0% fire fractional area. The upper, curved lines indicate index values at 1% fire fractional area.

The five NDI with the highest kappa values for each temperature range are shown in Tables 3–5. The top three kappa values in Table 3 were significantly higher than the lowest kappa value in Table 3 ( $p < 0.05$ ), but otherwise kappa values were not significantly different within Tables 3, 4 or 5. The bands shown in all three tables came from two specific wavelength ranges. The shorter wavelength band was always found between 2000 and 2071 nm, while the longer wavelength band was always found between 2399 and 2479 nm (Fig. 4). Furthermore, the shorter wavelength bands were always within one of

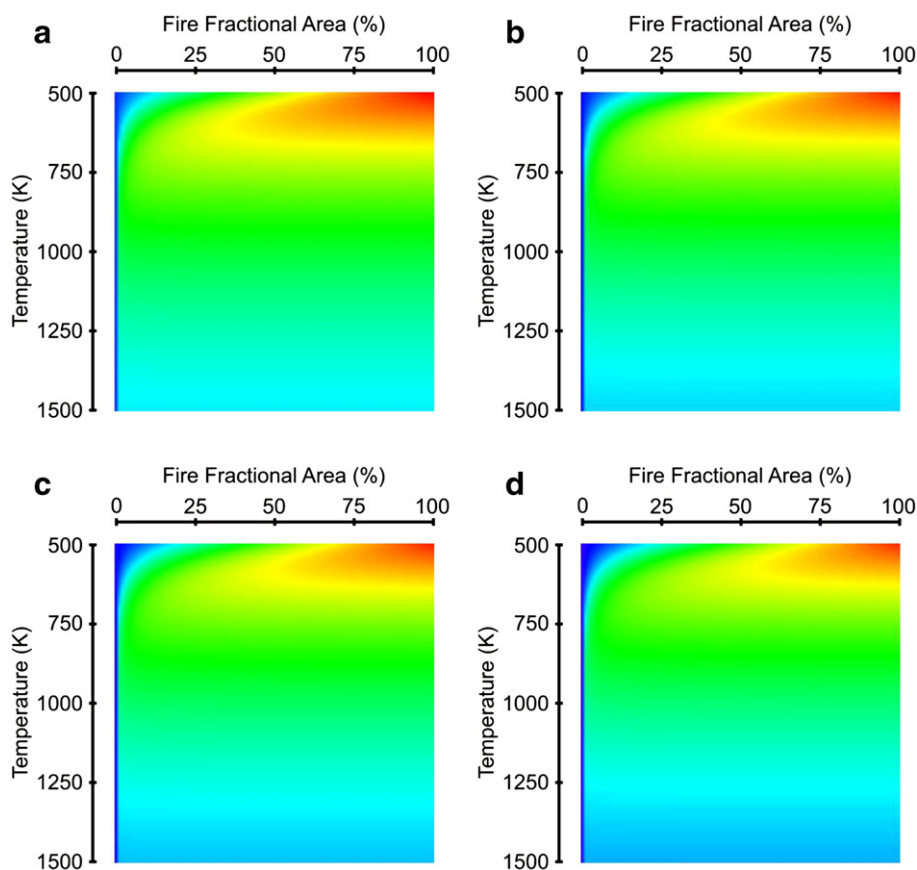


**Fig. 7.** HFDI values with varying elevation, modeled using MODTRAN. a) elevation = 0 km. b) elevation = 1 km. c) elevation = 2 km. d) elevation = 3 km. Scaling is shown on the color ramp in Fig. 6.

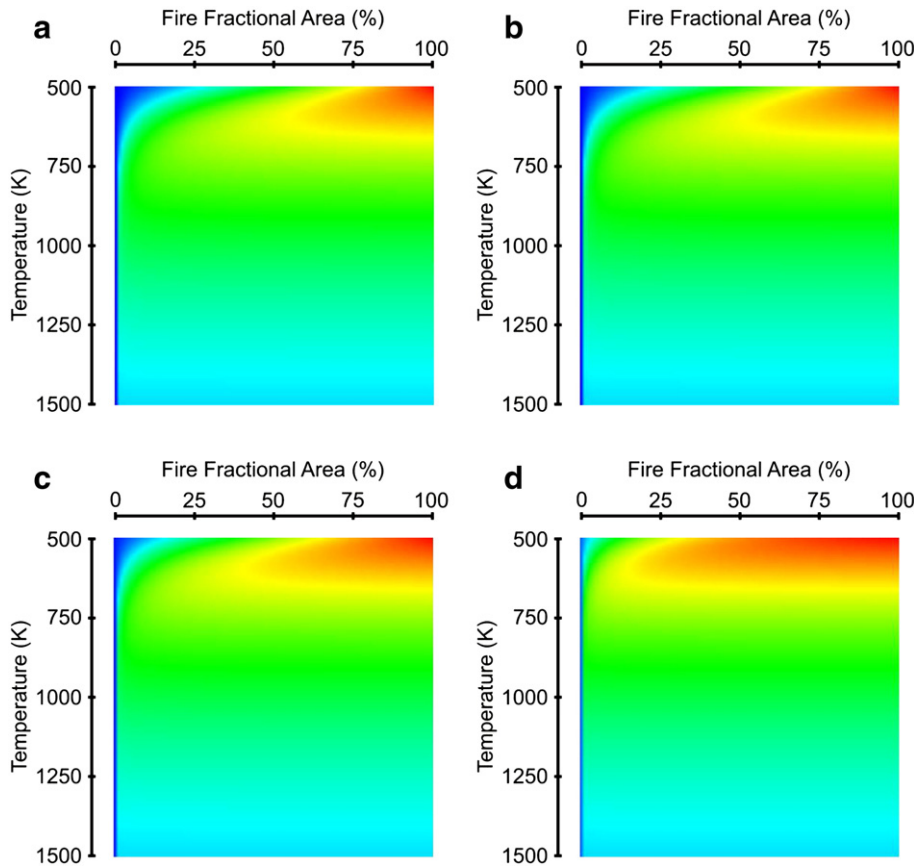


Fig. 9. HFDI values with varying solar zenith angle, modeled using MODTRAN. a) zenith angle = 0°. b) zenith angle = 25°. c) zenith angle = 50°. d) zenith angle = 75°. Scaling is shown on the color ramp in Fig. 6.

the carbon dioxide absorption features, while all but one of the longer wavelength bands was found outside of the absorption maxima between 2399 and 2479 nm. Both of the selected wavelength ranges are subject to water vapor absorption, although this absorption is generally stronger in the longer wavelength range.

The functionality of the indices listed in Tables 3–5 was the same. The longer wavelength bands have similar or lower reflected solar radiance compared to the shorter wavelength bands (Fig. 4). When emitted radiance is added to the background reflected solar radiance, total radiance in the longer wavelength range increases faster than total radiance in the shorter wavelength range. To allow the NDI values to increase with the presence of emitted radiance from fire, we used the longer wavelength as  $\lambda_1$  in Eq. (3). The threshold that produced the maximum kappa value for each NDI decreased as the temperature range decreased (Tables 3–5). The cooler fires contributed less emitted radiance, necessitating a lower threshold for accurate detection.

Due to the low kappa values for the NDI selected for temperatures less than 750 K, and the relatively small number of pixels in this temperature category (Table 1), we used the remaining two temperature categories to select a single NDI for further analysis. Only one NDI appears in both Tables 3 and 4. The NDI using bands 216 (2429 nm) and 179 (2061 nm) had the highest kappa value for temperatures below 1000 K, and the third highest kappa value for all temperatures. This index is also very similar to the top ranked NDI for all temperatures (Table 3). The NDI using bands centered on 2061 and 2429 nm is henceforth referred to as the Hyperspectral Fire Detection Index (HFDI). While we selected this NDI for further analysis, we expect that all of the indices listed in Tables 3–5 would perform similarly, as they use similar wavelengths.

The HFDI was applied to the Simi Fire AVIRIS scene (Fig. 5). The threshold value of  $-0.04$  from Table 3 was used for fire detection. Index values were lowest in unburned vegetation, due to greater liquid water absorption at 2429 nm. Index values were slightly higher in ash- and soil-covered areas within the fire scar. Differences in index values between burned and unburned areas indicate the impact of spectral reflectance on reflected solar radiance. The fire front is clearly

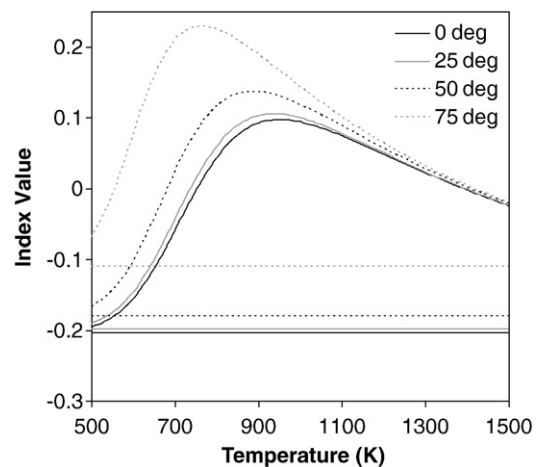
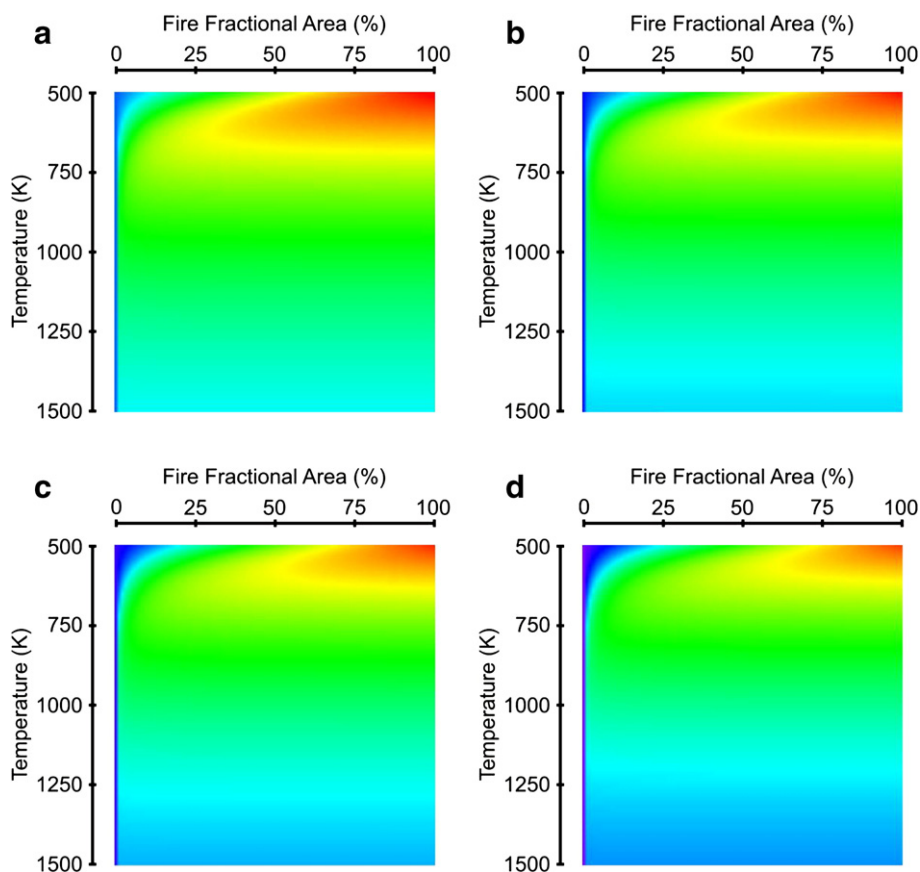


Fig. 10. HFDI values across a range of temperatures for solar zenith angles of 0, 25, 50, and 75 degrees. The lower, flat lines indicate index values at 0% fire fractional area. The upper, curved lines indicate index values at 1% fire fractional area.



**Fig. 11.** HFDI values with varying atmospheric water vapor concentration, modeled using MODTRAN. a) 500 atm cm. b) 1000 atm cm. c) 1500 atm cm. d) 2000 atm cm. Scaling is shown on the color ramp in Fig. 6.

visible in Fig. 5, and isolated trees still burning in riparian zones behind the fire front are visible upon close inspection.

#### 4.1. Index sensitivity

An ideal fire detection index would have a low value when no fire emission is present, and a rapid escalation in value with the presence of any fire emission within a pixel. MODTRAN simulations of the HFDI for the Simi Fire AVIRIS scene indicate that HFDI values do rapidly increase at low fire fractional area and moderately low temperature (Fig. 6). The background ash spectrum has an index value of  $-0.179$ . With a modeled blackbody emission temperature of 500 K, 15% of a pixel's area must be emitting before the index turns positive. At 600 K, only 3% of a pixel needs to have fire emission to turn the index positive, and by 680 K the fire fractional area drops to 1%. Interestingly, the index remains negative across all fire fractional areas for temperatures above 1410 K. Above this temperature, emitted radiance at 2061 nm increases faster than emitted radiance at 2429 nm, which keeps the index negative. Index values are highest at low temperatures and high fire fractional areas (Fig. 6).

Elevation, solar zenith angle, and atmospheric water vapor concentration are likely to impact the HFDI by altering atmospheric absorption in both of the index bands. For example, carbon dioxide is a strong absorber, so radiance in the 2061 nm band changes more rapidly with elevation than radiance in the 2429 nm band. While solar zenith angle does not impact emitted radiance, it could impact the background HFDI value through differential absorption and scattering at the index wavelengths. Finally, water vapor absorption is stronger at 2429 nm than 2061 nm, so atmospheric water vapor concentration can also impact index values. To evaluate the impacts of these factors on the HFDI, MODTRAN was used to evaluate

the sensitivity of HFDI to a change in elevation, solar zenith and atmospheric water vapor.

For the elevation simulations, the same aerial platform height of 5.6 km above sea level was maintained, but the ground elevation was varied between 0 and 3 km. Increased ground elevation reduces the path length for both the reflected solar radiance and the emitted radiance. Combined carbon dioxide and water vapor absorption at

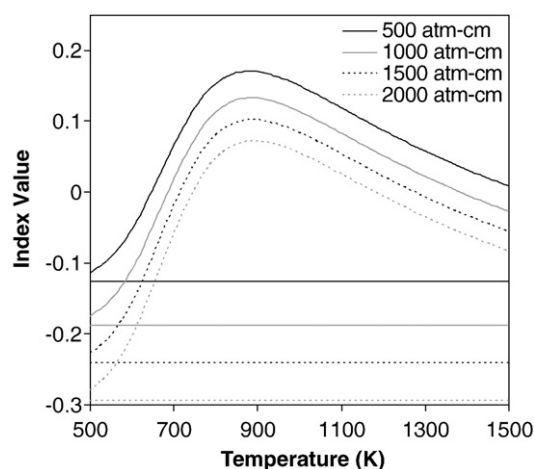


**Fig. 12.** HFDI values across a range of temperatures for atmospheric water vapor concentrations of 500, 1000, 1500, and 2500 atm cm. The lower, flat lines indicate index values at 0% fire fractional area. The upper, curved lines indicate index values at 1% fire fractional area.

2061 nm declined faster with increasing elevation than water vapor absorption at 2429 nm, resulting in reduced HFDI values. In Fig. 7, decreased HFDI values are most noticeable at low temperature and high fire fractional area. Modest decreases occur across the entire range of temperatures and fire fractional areas. Index sensitivity is most important at low fire fractional area. Fig. 8 compares background (0% fire coverage) and 1% fire coverage index values across all temperatures at the four modeled elevations. At temperatures below 600 K, there is some overlap between low elevation background index values and high elevation 1% fire cover index values.

Solar zenith angle only affects reflected solar radiance. Since reflected solar radiance is the dominant contributor to total radiance at low fire temperatures and fire fractional areas, high solar zenith angles can have an important impact on HFDI values. Fig. 9 reveals almost no difference in index values between solar zenith angles of 0° and 25°. As solar zenith angle increases to 50°, index values begin to visibly increase. At a solar zenith angle of 75°, index values are much higher relative to the 0° example (Fig. 9). Atmospheric attenuation is

stronger at shorter wavelengths, which reduces solar radiance at 2061 nm more rapidly than solar radiance at 2429 nm. Fig. 10 shows that background and 1% fire cover index values are nearly identical at 0° and 25°. Index values are markedly higher at 75°, but separation between the background and 1% lines is actually enhanced by the larger solar zenith angle. At temperatures below 660 K, there is overlap between the high solar zenith angle background and low solar zenith angle 1% fire cover index values.

Atmospheric water vapor has the greatest impact on index values. Water vapor absorption is stronger at 2429 nm, so increasing water vapor concentration decreases HFDI values (Fig. 11). High water vapor concentrations push the background index value to very low levels (Fig. 12). Water vapor has less of an impact on the 1% fire cover curves, because the emitted radiance has a shorter path length than the reflected solar radiance. At temperatures below 660 K, there is overlap between the 500 atm cm background and 2000 atm cm 1% fire cover index values. Impacts of elevation, solar zenith angle, and water vapor concentration on HFDI may prevent a universal threshold for fire detection under all conditions, but the sensitivity analysis demonstrates

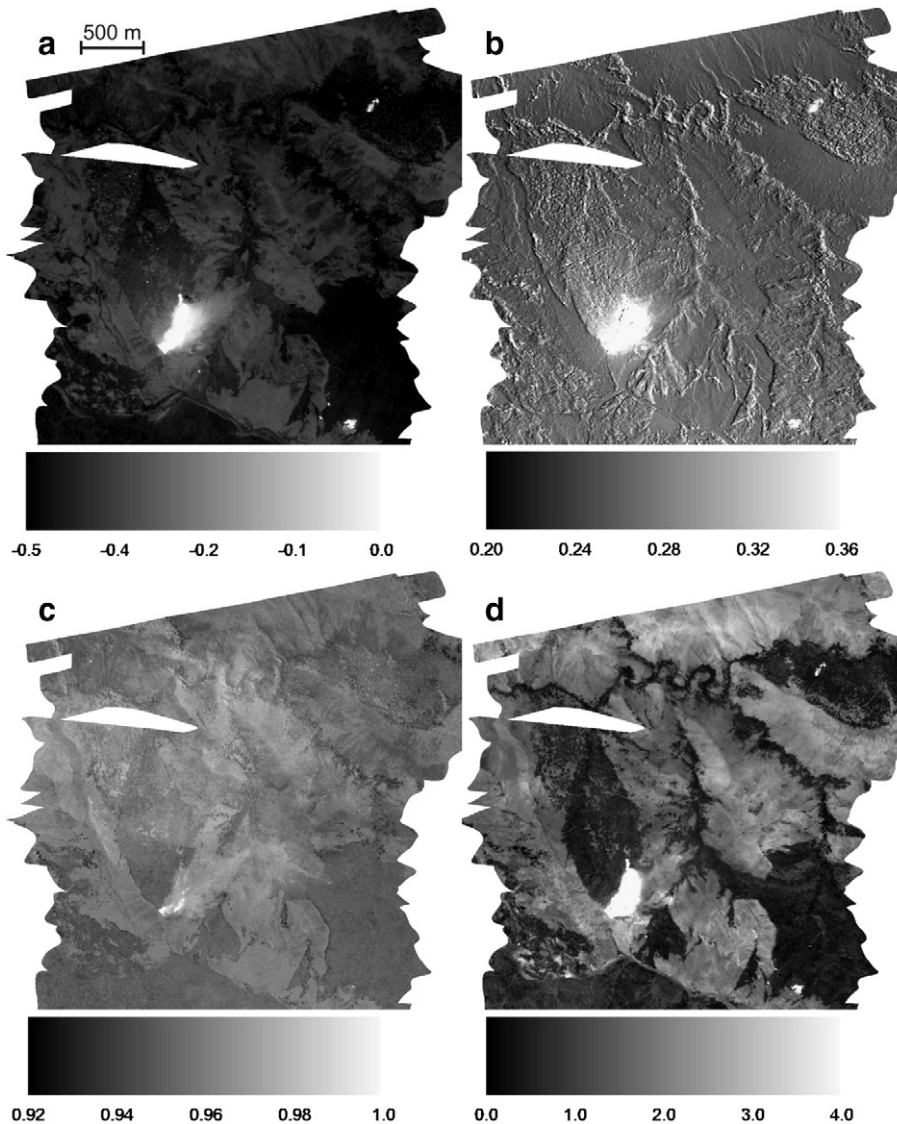


Fig. 13. A comparison of fire detection index values for an AVIRIS scene containing the 2007 Zaca Fire. a) HFDI using bands centered on 2424 nm and 2065 nm. b) Carbon dioxide absorption index. c) Potassium emission index. d) ASTER reflectance index.

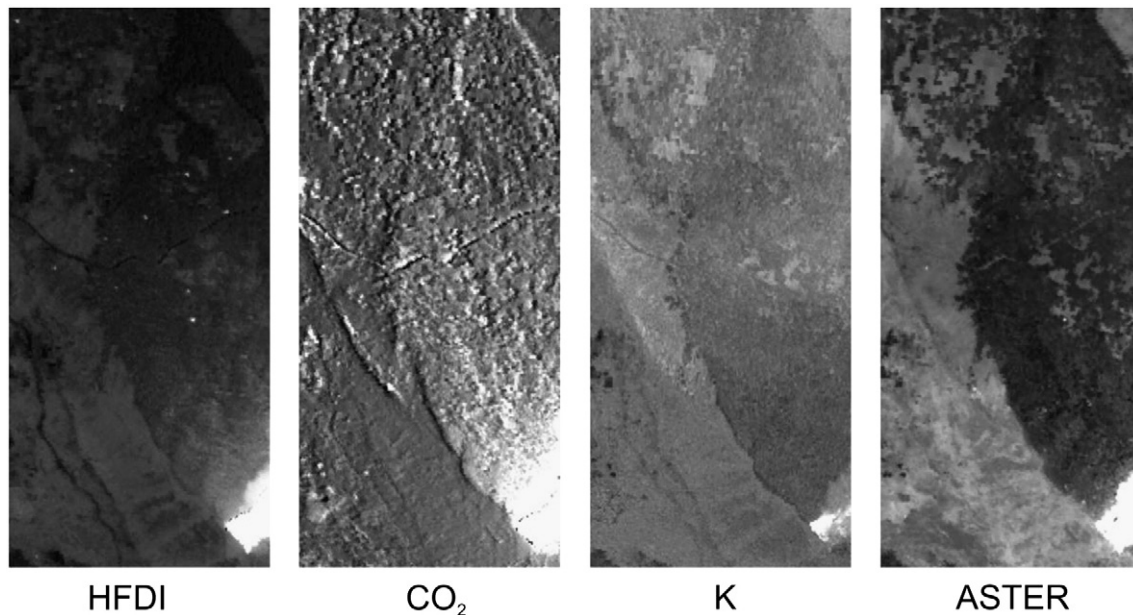


Fig. 14. Magnified subsets of the four fire detection index images shown in Fig. 13.

that separation between the background and 1% fire cover index values is maintained across the entire range of tested conditions.

#### 4.2. Qualitative index comparison

We tested the HFDI on two previously unmodeled AVIRIS scenes containing fire. For each of the new AVIRIS scenes, we selected the bands closest to those selected for the Simi Fire scene. Since AVIRIS band center wavelengths change from year to year, the bands and wavelengths used for these scenes differ slightly from those used for the Simi Fire scene. HFDI images were compared with images for the Vodacek et al. (2002) potassium emission index, the Dennison (2006) carbon dioxide absorption index, and the Morisette et al. (2005b) ASTER reflectance index. For the 2007 Zaca Fire scene, bands centered on 2424 nm and 2065 nm were used to calculate HFDI. All four indices had high values in the largest burning area in the AVIRIS scene (Fig. 13). The HFDI and the carbon dioxide index detected two smaller fires on the right side of the scene, which the potassium index missed. The carbon dioxide index has a large number of high value false detections that correspond to variation in background land cover. ASTER index values were elevated within the fire scar due to ash and soil surfaces with higher reflectance in the shortwave infrared relative to the near infrared. In many areas the fire scar had an index value greater than 2, the threshold used by Morisette et al. (2005b) for fire detection. In comparison to the carbon dioxide and ASTER indices, HFDI has relatively little background variation. In the magnified section of the scene (Fig. 14), HFDI detects several “hot pixels” that may correspond to spot fires, while neither of the other hyperspectral indices detects these fires.

The HFDI also outperforms the potassium and carbon dioxide indices in the 2008 Indians Fire AVIRIS scene (Fig. 15). HFDI for this scene was calculated using bands centered on 2428 nm and 2058 nm. Little of the fire is detected by the potassium emission index due to heavy smoke obscuring emitted radiance in the near infrared. The carbon dioxide absorption index does pick out the fire front, but with greater background variation. The HFDI and ASTER index images appear quite similar, but do exhibit a few important differences. HFDI displays more smoke contamination in the active section of the fire close to the bottom of the image, while the ASTER index shows

elevated index values for the fire scar in the non-burning section near the top of the image. In a magnified section of the scene (Fig. 16), HFDI reveals much more detail on the locations of possible spot fires compared with the other indices.

#### 5. Discussion

The HFDI is best suited to detecting fires at temperatures between 750 and 1400 K. Below 750 K, kappa values for all tested NDI were relatively low. Overlap in HFDI values with changing elevation, solar zenith angle, and atmospheric water vapor concentration is also possible at temperatures below 700 K. Temperatures below 700 K are indicative of smoldering combustion while flaming combustion starts at temperatures higher than 700 K (Pyne et al., 1996; Dennison et al., 2006). The HFDI thus may be most appropriate for the detection of flaming combustion, but may not be able to reliably detect smoldering. However, due to the low emitted radiance in the shortwave infrared in the 500–700 K range, reliable detection of smoldering combustion may not be possible using simple hyperspectral indices such as a NDI. An approach that integrates total radiance over many bands could be more successful. HFDI values were low for temperatures in excess of 1400 K due to increased emitted radiance at 2061 nm. Fire temperatures exceeding 1400 K should be relatively uncommon. In the Dennison et al. (2006) temperature modeling of the Simi Fire, only 0.15% of pixels modeled with an emitted radiance had a temperature in excess of 1400 K. Fire detection at the highest possible temperatures may require a complementary approach to the HFDI. A complementary index could use a high threshold value for single band or integrated shortwave infrared radiance to detect high temperature fires that HFDI is likely to miss.

The sensitivity analysis revealed that there is unlikely to be a single universal HFDI threshold for fire detection. Still, practical guideline values can be set. Positive HFDI values are a strong indicator of the presence of fire within a pixel. HFDI values above  $-0.1$  represent a likely detection of fire, but background HFDI values and potential impacts of elevation, solar zenith angle, and water vapor must be taken into account. Further work is needed to quantify the impact of background reflectance spectra on the HFDI. Live vegetation and ash/bare soil had different index values due to differences in spectral

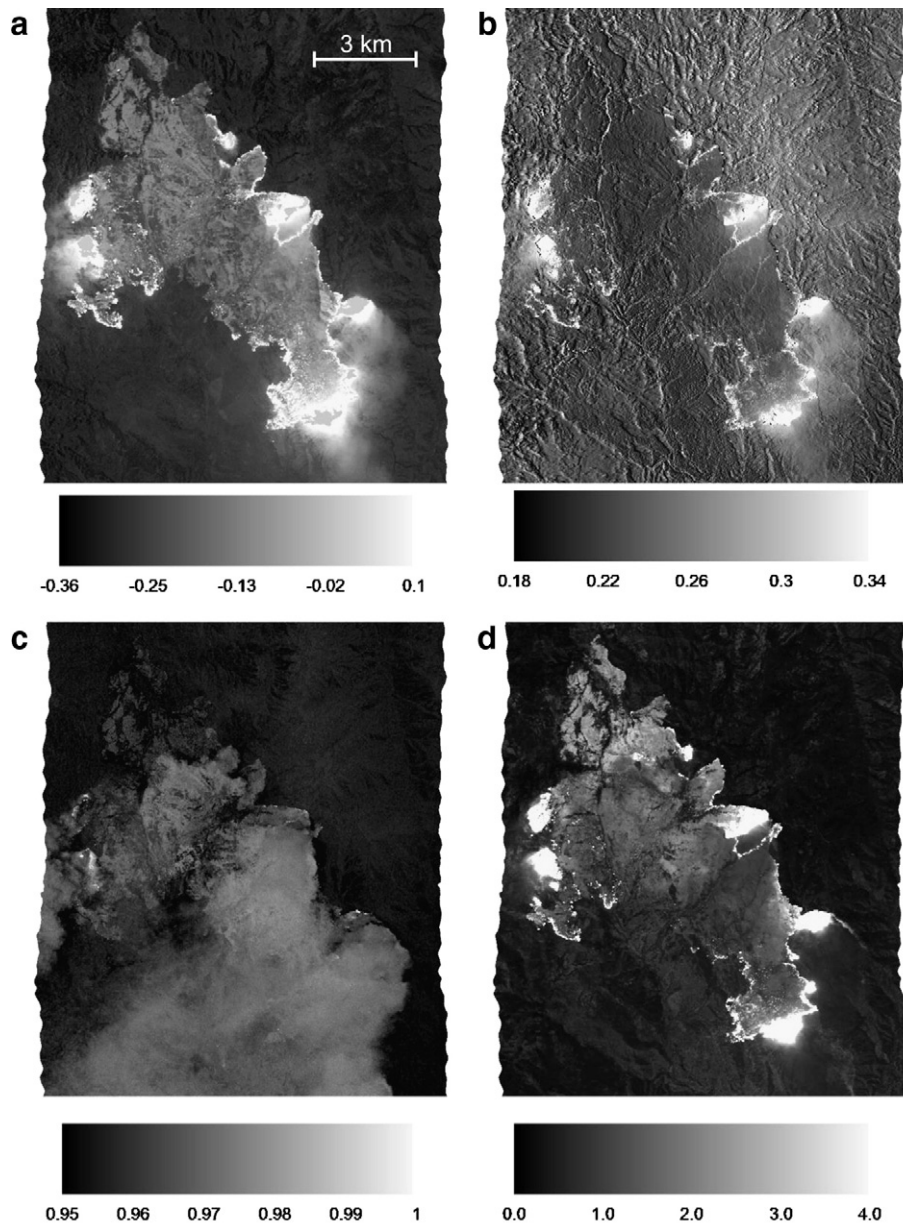


**Fig. 15.** A comparison of HFDI values for an AVIRIS scene containing the 2008 Indians Fire. a) HFDI using bands centered on 2428 nm and 2058 nm. Gray pixels in the center of the highest emission areas (e.g. left side, center) indicate band saturation. b) Carbon dioxide absorption index. The area of saturation for this index is similar to (a). c) Potassium emission index. d) ASTER reflectance index. The area of saturation for this index is also similar to (a).

reflectance. Our sensitivity analysis used an ash spectrum with an apparent surface reflectance of 31.7% in both index bands. Darker background surfaces and surfaces that have decreasing reflectance with wavelength (e.g., vegetation) will enhance fire detectability. Brighter background surfaces and surfaces that have increasing reflectance with wavelength could decrease fire detection accuracy.

Water vapor concentration had the greatest impact on HFDI values, due to stronger water vapor absorption at 2429 nm relative to 2061 nm. To minimize index sensitivity to changing atmospheric water vapor concentrations, the HFDI could be altered to use two bands with more similar water vapor absorption coefficients. The sensor response functions of hyperspectral sensors vary from sensor to sensor and even from year to year on some sensors. Optimal bands with similar water vapor absorption coefficients would ideally be selected for individual instrument sensor response functions. Our MODTRAN simulations showed that 2003 AVIRIS bands centered at 1990 nm and 2399 nm have similar water vapor absorption. The kappa value for this

band combination was moderately lower for all fire temperatures (0.777), but this small sacrifice in accuracy might be acceptable for gained versatility under varying atmospheric water vapor concentrations.

While we compared our fire detection results with fire temperature mapped using a different hyperspectral technique, a lack of “ground truth” data on fire locations prevented a true quantitative accuracy assessment of fire detection. Further research is needed to quantify accuracy, especially to determine thresholds that minimize false fire detection. False detection could occur for background materials with high shortwave infrared reflectance or sharply lower 2061 nm reflectance compared to 2429 nm reflectance. The circumstances under which false detection can occur should be further investigated.

Index sensitivity to fire fractional area was only tested for fractional area greater than 1%. Fire detection limits are likely to scale with changes in the spatial resolution of the sensor. Thus as the ground instantaneous field of view increases, the minimum size of fire

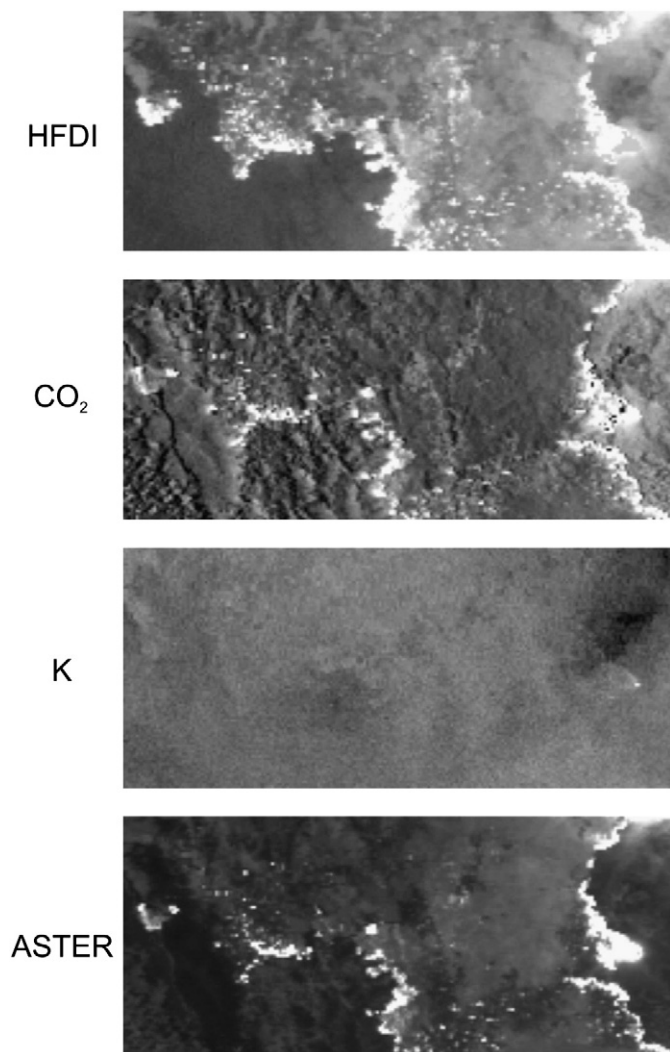


Fig. 16. Magnified subsets of the four fire detection index images shown in Fig. 15.

required for detection is also likely to increase. We have demonstrated that HFDI is able to detect fires at spatial resolutions of 4 and 16 m. More investigation is needed to determine how HFDI will function at coarser spatial resolutions used for existing (e.g., Hyperion) and proposed spaceborne hyperspectral sensors.

## 6. Conclusions

Our findings verify the utility of hyperspectral shortwave infrared data for fire detection. Bands centered near 2061 and 2429 nm provided high accuracy detection of fire within the Simi Fire AVIRIS scene. While HFDI was sensitive to variable elevation, solar zenith angle, and atmospheric water vapor concentration, separation between background and fire HFDI values was preserved across the entire range of fire temperature. HFDI will be useful as a stand-alone fire detection algorithm and as a preprocessing step for more complex hyperspectral fire temperature retrieval algorithms (e.g., Dennison

et al., 2006). Since fires typically cover less than 10% of a scene, HFDI could potentially decrease temperature retrieval run time by 90% or more. This type of improvement in hyperspectral fire temperature retrieval will be necessary for expeditious application to future spaceborne hyperspectral data.

## References

- Berk, A., Bernstein, L. S., & Robertson, D. C. (1989). *MODTRAN: A Moderate Resolution Model for LOWTRAN7*, AFGL-TR-89-0122. MA: Hanscom Air Force Base.
- Cohen, J. (1960). A coefficient of agreement for nominal scales. *Educational and Psychological Measurement*, 20, 37–46.
- Congalton, R. (1991). A review of assessment the accuracy of classifications of remotely sensed data. *Remote Sensing of Environment*, 37, 35–46.
- Csiszar, I., Morisette, J., & Giglio, L. (2006). Validation of active fire detection from moderate resolution satellite sensors: the MODIS example in Northern Eurasia. *IEEE Transactions on Geoscience and Remote Sensing*, 44, 1757–1764.
- Dennison, P. E. (2006). Fire detection in imaging spectrometer data using atmospheric carbon dioxide absorption. *International Journal of Remote Sensing*, 27, 3049–3055.
- Dennison, P. E., Charoensiri, K., Roberts, D. A., Peterson, S. H., & Green, R. O. (2006). Wildfire temperature and land cover modeling using hyperspectral data. *Remote Sensing of Environment*, 100, 212–222.
- Giglio, L., Csiszar, I., Restas, A., Morisette, J. T., Schroeder, W., Morton, D., & Justice, C. O. (2008). Active fire detection and characterization with the advanced spaceborne thermal emission and reflection radiometer (ASTER). *Remote Sensing of Environment*, 112, 3055–3063.
- Giglio, L., Desloires, J., Justice, C. O., & Kaufman, Y. J. (2003). An enhanced contextual fire detection algorithm for MODIS. *Remote Sensing of Environment*, 87, 273–282.
- Green, R. O. (1996). Estimation of biomass fire temperature and areal extent from calibrated AVIRIS spectra. *Summaries of the Sixth Annual JPL Airborne Earth Science Workshop, Pasadena: Jet Propulsion Laboratory, vol. 1*. (pp. 105–113): JPL Publication 96-4.
- Green, R. O., Eastwood, M. L., Sarture, C. M., Chrien, T. G., Aronsson, M., Chippendale, B. J., Faust, J. A., Pavri, B. E., Chovit, C. J., Solis, M. S., Olah, M. R., & Williams, O. (1998). Imaging spectroscopy and the Airborne Visible Infrared Imaging Spectrometer (AVIRIS). *Remote Sensing of Environment*, 65, 227–248.
- Ichoku, C., Kaufman, Y. J., Giglio, L., Li, Z., Fraser, R. H., Jin, J. Z., & Park, W. M. (2003). Comparative analysis of daytime fire detection algorithms using AVHRR data for the 1995 fire season in Canada: perspective for MODIS. *International Journal of Remote Sensing*, 24, 1669–1690.
- Kaufman, Y. J., Justice, C. O., Flynn, L. P., Kendall, J. D., Prins, E. M., Ward, D. E., Menzel, W. P., & Setzer, A. W. (1998). Potential global fire monitoring from EOS-MODIS. *Journal of Geophysical Research*, 103, 32215–32238.
- Kaufman, Y. J., Tucker, C. J., & Fung, I. (1990). Remote sensing of biomass burning in the tropics. *Journal of Geophysical Research*, 95, 9927–9939.
- Morisette, J. T., Giglio, L., Csiszar, I., & Justice, C. O. (2005). Validation of the MODIS active fire product over Southern Africa with ASTER data. *International Journal of Remote Sensing*, 26, 4239–4264.
- Morisette, J. T., Giglio, L., Csiszar, I., Setzer, A., Schroeder, W., Morton, D., & Justice, C. O. (2005). Validation of MODIS active fire detection products derived from two algorithms. *Earth Interactions*, 9(9), 1–25.
- Prins, E. M., & Menzel, W. P. (1992). Geostationary satellite detection of biomass burning in South America. *International Journal of Remote Sensing*, 13, 2783–2799.
- Pyne, S. J., Andrews, P. L., & Laven, R. D. (1996). *Introduction to wildland fire*. New York: Wiley.
- Roberts, D. A., Gardner, M., Church, R., Ustin, S., Scheer, G., & Green, R. O. (1998). Mapping chaparral in the Santa Monica Mountains using multiple endmember spectral mixture models. *Remote Sensing of Environment*, 65, 267–279.
- Schroeder, W., Prins, E., Giglio, L., Csiszar, I., Schmidt, C., Morisette, J., & Morton, D. (2008). Validation of GOES and MODIS active fire detection products using ASTER and ETM+ data. *Remote Sensing of Environment*, 112, 2711–2726.
- Thomas, P. J., & O. N. (1993). Near-infrared forest fire detection concept. *Applied Optics*, 32, 5348–5355.
- Vodacek, A., Kremens, R. L., Fordham, A. J., Vangorden, S. C., Luisi, D., Schott, J. R., & Latham, D. J. (2002). Remote optical detection of biomass burning using a potassium emission signature. *International Journal of Remote Sensing*, 13, 2721–2726.
- Wang, L., & Qu, J. J. (2007). NMDI: a normalized multi-band drought index for monitoring soil and vegetation moisture with satellite remote sensing. *Geophysical Research Letters*, 34, L20405.
- Wang, L., Qu, J. J., & Hao, X. (2008). Forest fire detection using the normalized multi-band drought index (NMDI) with satellite measurements. *Agricultural and Forest Meteorology*, 148, 1767–1776.